MECHANICS OF PERIODIC ELASTOMERIC STRUCTURES WITH VARYING VOID VOLUME FRACTION AND THIN-FILM COATING

by

Michael C. Kozlowski

Submitted to the Department of Mechanical Engineering
in partial fulfillment of the requirements for the degree of

BACHELOR OF SCIENCE IN MECHANICAL ENGINEERING

at the

MASSACHUSETTS INSTITUTE OF TECHNOLOGY

JUNE 2008

Author . . . . . .

Department of Mechanical Engineering
May 9, 2008

Certified by . . . . . .

Mary C. Boyce
Kendall Family Professor of Mechanical Engineering
Thesis Supervisor

Accepted by . . . . . .

John H. Lienhard V
Professor of Mechanical Engineering
Chairman, Undergraduate Thesis Committee

MECHANICS OF PERIODIC ELASTOMERIC STRUCTURES WITH VARYING VOID VOLUME FRACTION AND THIN-FILM COATING

by
Michael C. Kozlowski

Submitted to the Department of Mechanical Engineering
on May 9, 2008, in partial fulfillment of the
requirements for the degree of
BACHELOR OF SCIENCE IN MECHANICAL ENGINEERING

Abstract

Super-elastic periodic structures possess special mechanical, photonic, phononic, and topological properties, making them particularly relevant for application at the micro and nano length scales. This study examines the behavior of such materials in two and three dimensions when void volume fraction is varied and a thin-film coating is incorporated. Computer modeling was used to predict and understand the mechanics of the transformation behavior; results showed that three-dimensional specimens behaved like their 2D counterparts and that addition of the film influenced structural transformation. Specifically, increasing volume fraction brought pattern transformation at lower values of stress and strain. Conversely, film presence postponed transformation and made it a gradual process. The film also showed considerable out-of-plane displacement and created a channel which spanned the structure. Out-of-plane motion and pattern transformation were verified experimentally by loading a 90 x 110 mm specimen to a strain of about 13% using a testing fixture. Although conducted in the macroscopic domain, experimental behavior can be expected at smaller length scales. The transformations and the surface topology alterations are reversible upon unloading, giving the ability to use deformation as a means of tuning or switching wave propagation properties that depend on periodicity, and surface properties that depend on topology.

Thesis Supervisor: Mary C. Boyce
Title: Gail E. Kendall Professor of Mechanical Engineering

Contents

1 Introduction

The study of elastomeric periodic structures is motivated by their special mechanical, wave, and textural properties, and relevance for nano- and micro-scale devices. Mechanically speaking, these patterns show super-elastic behavior before a critical stress value after which strain occurs at nearly constant stress. Such behavior makes them ideal energy absorbers; circular honeycomb structures, for example, have already been evaluated for this purpose [1, 2]. If the array-pattern length scales are on the order of the wavelength of light, the structures can alter the propagation of electromagnetic waves. In this case, the number of practical applications can be enormous: LEDs, optical filters, nanoscopic lasers, ultrawhite pigment, radio frequency antennas/reflectors, and photonic integrated circuits, to name a few [3]. The iridescence seen in butterflies, beetles, moths, birds, and fish also functions by this mechanism [4, 5, 6, 7] . Similarly, audible tuning can be achieved if the structures are set to the appropriate scale. Sound filters could be created by blocking specified frequency ranges [8]; acoustical mirrors or wave guides could also be implemented. Adding a thin-film layer to the periodic structures could add further functionality. Deformation induced topology changes could be useful in microfluidics [9, 10] or to create super-hydrophobic surfaces [11]. Other potential applications are release-on-command coatings [12] and adhesives [13, 14, 15, 16], controllable frictional change [17, 18], and use in chemical sensing [19, 20, 21].

This study concerns two- and three-dimensional periodic structures of elastomeric materials. The structures are created from an elastomer, PSM-4 [22], and have square patterns of circular holes. Upon loading to a critical buckling stress, the circle-to-circle ligaments buckle, causing a repeatable and reversible pattern transformation throughout [23]. Among the 2D and 3D specimens considered, void volume fraction (ϑ_f, the ratio of void volume to material volume) and representative volume element (RVE) size are varied. Volume fractions considered are 0.20, 0.59, and 0.70 while RVEs range in array size from 2x2 to 10x10. In addition to stand-alone specimens, periodic and random-void structures with a thin-film layer of PSM-4 were examined. Computer modeling captured behavioral predictions and experimentation was used for validation. Although conducted in the macroscopic domain, transformation behavior can be expected at smaller length scales.

Patterning at such levels is now possible with techniques such as micro-fabrication [24, 25] and interference lithography [26, 27, 28, 29, 30, 31]. With reliable manufacturing processes, successful implementation now requires a thorough understanding of behavior. Thus, the goals of this study are to model and interpret transformation behavior for 2D, 3D, and thin-film structures and to verify the predictions experimentally.

2 Modeling

Computer modeling using nonlinear finite element analysis was utilized to study the simulated behavior of the elastomeric structures of interest. Two-dimensional patterns of variable void-volume fraction (ϑ_f, the ratio of void volume to material volume) and matrix size were first studied for their predictability and relative modeling simplicity. Next, a third dimension was added to all 2D cases so that behavior of more practical specimens could be examined. Once 3D transformation was fully comprehended, a thin film was added to one of the voided faces for each 3D structure. This film was of the same material as the structure: An elastomer called PSM-4 manufactured by the Measurements Group [22]. The modeling parameters used for PSM-4 were 3.25 MPa for the modulus and 0.4999 for the Poisson ratio. It was predicted that the non-film 3D structures would behave as their 2D counterparts, while addition of the film would render interesting contours but would not drastically affect transformation of the underlying structure.

2.1 2D Periodic Structures of Varying Void-Volume Fraction

The modeling and analysis package ABAQUS/CAE was used in conjunction with MATLAB to render visualizations and output data for the 2D models. To start, the CAE component of ABAQUS was used to model and mesh the specimens. A MATLAB "Analysis Input Writer" script (Bertoldi K., private communication) then read in the mesh definitions and added additional input such as boundary and loading conditions. Finally, the ABAQUS compiler output a visualization database as well as output data after being passed the Input Writer file.

This modeling process was followed to study the various 2D array configurations. Using CAE, three 9.97 mm square base units containing circular voids (Fig. 1) were constructed with different ϑ_f. In the 2D case, ϑ_f is given by, $\pi D^2/4L^2$, where D is the void diameter and L measures the sides of the square. By enlarging the circular void, the ϑ_f was increased from 0.20 to 0.59, and finally to 0.70. For each of the base units, array sizes from 2x2 to 10x10 were constructed, giving twenty-

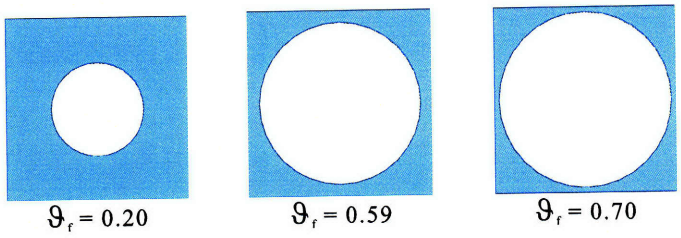

Figure 1: The 2D base units of void volume fraction 0.20, 0.59, and 0.70. The square dimensions are 9.97 x 9.97 mm.

seven array configurations. Examples of meshed 2x2 and 10x10 arrays of ϑ_f=0.59 are shown in Fig. 2. All array configurations were meshed in CAE using 6-node, triangular, quadratic, hybrid, plane-strain elements (type CPE6H). Given the void curvature of the base units, the triangular elements provided a superior fit over the standard "quad" type; the mesh element order was chosen as quadratic to provide more accurate approximations. The nine array sizes for each void-volume

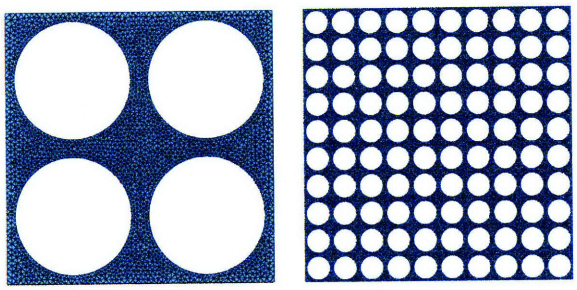

Figure 2: Meshed 2x2 and 10x10 arrays of ϑ_f=0.59 and element type CPE6H. Note that the figure is not to scale: The array on the right can be constructed using a 5x5 pattern of the array on the left.

category were constrained with infinite periodic boundary conditions before examination with eigen analysis. A representative size (2x2) from each void-volume designation was also subjected to post-transformational analysis.

2.1.1 Material Behavior

Stress-strain tests were previously conducted to characterize matrix material behavior [3]. Specimens were subjected to uniaxial compression at constant nominal strain rates of 0.05 and 0.005 $\frac{1}{s}$ with a Zwick screw-driven testing device. Results showed typical elastomer behavior: Strain-rate independence and negligible hysteresis during loading-unloading. Additionally, the initial modulus was found to be 3.25 MPa. To predict material behavior, a two-term Rivlin approximation was used with incompressibility. As shown in Fig. 3 (for a strain rate of 0.05 $\frac{1}{s}$), this approach was in agreement with the experimental data through to 40% strain.

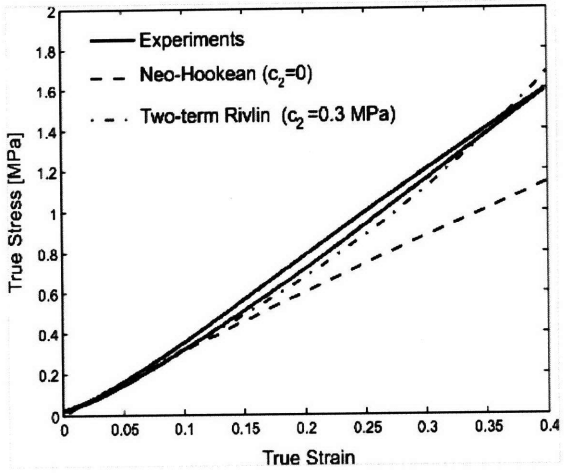

Figure 3: Uniaxial compression stress-strain data for PSM-4 at a constrain strain-rate of 0.05 $\frac{1}{s}$. The two-term Rivlin approximation tracked the data through to 40% strain. *Image borrowed from Bertoldi et. al, 2007 [3].*

2.1.2 Boundary Conditions for Infinite Periodic Structures

Both finite and "infinite" specimens were loaded, constrained, and analyzed after proper coding of the Input Writer. To identify the differences between these two boundary conditions, consider the case of a square, bi-material (modulus ratio $E_1/E_2 = 2$), 10x10 array, shown in Fig. 4, where elements were randomly assigned a modulus of either E_1 or E_2. The finite condition on the left was created by (a) pinning the lower left node, (b) constraining the bottom and top edges

on rollers, and (c) imposing a strain of -10% in the vertical direction, leaving the lateral edges traction- and constraint-free. From the figure, it can be seen that both the top and bottom edges appear horizontal and that the vertical edges are non-symmetric. From this simulation it is clear

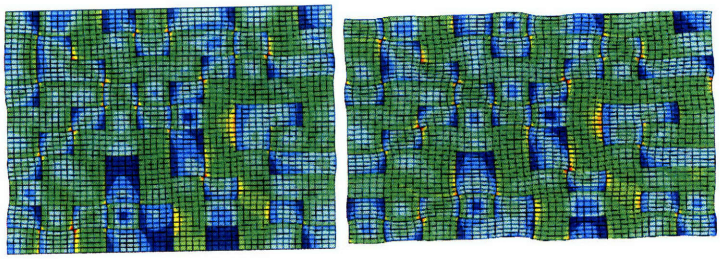

Figure 4: A square 10x10 finite (left) and infinite (right) bi-material ($E_1/E_2 = 2$) specimen displaced to -10% and -30% strain, respectively. The infinite specimen was strained further to exaggerate the periodic boundary conditions.

that the resulting deformation of the structure is strongly influenced by its boundary conditions (note, for example, the straightness of the roller edges). To eliminate boundary impact and model the structure as though it was cut from an infinitely repeating microstructure, periodic boundary conditions were imposed upon the other specimen of Fig. 4. Additionally, the structure was pinned at the lower left node to prevent rigid body motion. After -30% strain, the visualization shows the unique pattern resulting from the boundary conditions. The top-bottom and left-right relationships are symmetrically inverted, meaning that the right edge would fit onto the left edge and the bottom edge would mate with the top. The complete structure now serves as a repeating unit, capable of fitting together with copies of itself to form an infinite structure. More formally, periodic boundary conditions are imposed following

$$u_1|_B - u_1|_A = \frac{\partial u_1}{\partial X_1}(X_1|_B - X_1|_A) + \frac{\partial u_1}{\partial X_2}(X_2|_B - X_2|_A)$$
$$u_2|_B - u_2|_A = \frac{\partial u_2}{\partial X_1}(X_1|_B - X_1|_A) + \frac{\partial u_2}{\partial X_2}(X_2|_B - X_2|_A),$$

where A and B are periodic pair points located on the element boundaries (left-right and top-bottom pairs) and u_1, u_2 denote displacement in X_1, X_2, the coordinate positions in the undeformed mesh [32]. The application of macroscopic loading is done operationally through a set of virtual nodes. Consequently, the nominal stress of the representative volume element (RVE) is found by dividing

the reaction force at the loaded virtual node by the volume of the RVE, while the nominal strain experienced by the RVE is simply equal to the displacement of the virtual node.

2.1.3 Refined Eigen Analysis

Once the periodic boundary conditions of the RVEs were prescribed, the structures were analyzed using eigen value analysis. Specimens were first constructed as RVEs with pY x pY periodicity (where Y serves as the primitive cell) and infinite periodic boundary conditions. Critical stress values were defined as the infimum over which instability occurs, and were applied to all cells [3]. This process gives eigen values and modes for structural instability of the specimen microstructure; here, the expected instabilities will arise due to inter-void ligament buckling [23]. The analysis was implemented numerically using the *BUCKLE module of ABAQUS; it performs a linear perturbation procedure which outputs an eigen mode (corresponding to the resulting buckled array pattern) and value (the critical buckling stress level) for requested modes. To show that specific buckled patterns would repeat for larger RVE sizes, eigen analysis was performed on sizes up to 10x10. This procedure was carried out for each volume fraction.

2.1.4 Post-Transformation Analysis

To capture force-displacement (and thus stress-strain behavior) for the elastomeric arrays , a post-transformation analysis was conducted. This separate step was required due to the operational characteristics of the ABAQUS environment. The *BUCKLE module exploits material instability and captures eigen mode deformation, but only presents end-state data (eigen mode and value). A standard loading analysis, on the other hand, gives progressive data (i.e. force and displacement throughout loading) but does not capture bifurcation. Thus, to generate incremental force-displacement information for bifurcation, an imperfection was introduced to the loaded mesh. This imperfection was programmed to perturb the mesh by a small amount in the direction of the first buckling mode by using buckled nodal coordinates from the eigen analysis. The imperfection was

defined as

$$\Delta x_0 = w\frac{d_x + d_y}{2}\phi_1.$$

Thus, the perturbation is simply an average of the vertical (d_y) and horizontal (d_x) center-to-center void spacing scaled by the factor w; ϕ_1 denotes the first buckling mode. In each post-transformational analysis, w=0.5% while d_x and d_y were both equal to 9.97 mm.

2.2 3D Periodic Structures of Varying Void-Volume Fraction

To study the three-dimensional behavior of the periodic arrays, the 2D cases described in Section 2.1 were simply constructed in 3D, with the third dimension, the thickness, being 9.4 mm. The 3D structures were infinite and periodic in the x-y plane, but were finite in z. The same modeling sequence was used and similar constraints were imposed: A corner node was pinned to prevent rigid-body motion and both voided surface were constrained to their plane; all other surfaces were constraint- and traction-free. Infinite periodic boundary conditions were applied for all simulations; eigen analysis was again used for buckling data while post-transformational analysis was implemented to study the stress-strain behavior. Wedges of type C3D15H (15 node, hybrid, quadratic triangular prism)–the 3D analog of the 2D triangles–were selected as mesh elements. Unlike the 2D cases, the 3D structures ranged in size from 2x2 to 6x6 and volume fractions studied were 0.59 and 0.70 (since the 0.20 fraction did not exhibit buckling).

2.3 3D Periodic Structures with Thin-Film Coating

Structures possessing the thin-film coating were found to result in simulation convergence issues regarding the instability analysis where anomalous surface perturbations were activated. To develop a functional simulation, the post-transformational perturbation technique (Section 2.1.4) was applied: The 3D structure containing the film was perturbed by a small imperfection corresponding to the transformation pattern of the structure without a coating, and was then loaded to the specified strain level. The imperfection was imposed using nodal information from the corresponding

buckled non-film 3D structure. This method was successful in providing stress-strain behavior but did not, a priori, predict the transformation pattern. The 3D film specimens were all pinned at one corner and were constrained to the z=0 plane along the non-film surface. These simulations continued with ϑ_f 0.59 and 0.70, but were only obtained for sizes 2x2, 3x3, and 4x4 due to computing limitations.

2.4 3D Film Structure with Randomly Located Voids

A three-dimensional film structure of volume fraction 0.50 was created with randomly located voids. The edges were set to satisfy periodicity and the minimum allowable ligament thickness was selected as 1.3 mm, that for ϑ_f=0.59. The top edge had three one-quarter-area circles cut from it, mating with three three-quarter-area circles on the bottom edge. Similarly, the left and right edges each possessed two half-circle cuts. The overall structure measured 39.88 x 39.88 mm in the x-y plane (the dimensions for a 4x4 periodic structure) and 9.4 mm in the z-direction; it was constrained by pinning a node and requiring the bottom and back (non-film) surfaces to remain in-plane. The structure was subject to pure uniaxial compression to strain levels of 10 and 20%.

3 Modeling Results

Simulations predicting behavior of the periodic elastomeric structures were successfully completed for the 2D, 3D, and 3D film cases. Data from the eigen analysis were used to plot critical buckling stress (eigen value) against RVE size, and post-transformation output yielded stress-strain curves. Buckling information was not obtainable for the 3D film specimens (since the film surface could not be constrained), but the imperfection-perturbation technique (Section 2.1.4) allowed uniaxial compression into the first mode shape. Stress-strain plots, contour maps, and cross-sectional slices were created from the force-displacement data.

3.1 2D Periodic Structures of Varying Void-Volume Fraction

Presented here are visualizations and plots which capture transformation behavior for the 2D periodic patterns of ϑ_f 0.20, 0.59, and 0.70 and RVE size 2x2 to 10x10. Graphics showing transformed patterns for the different volume fractions are included for qualitative comparison between the groups. Plots of critical buckling stress vs. RVE size are also given so that trends of buckling stress can be viewed as the periodicity grows. Finally, the stress-strain plots for volume fractions 0.59 and 0.70 capture bifurcation clearly, while that for volume fraction 0.20 indicates that a buckling instability does not occur.

A sample visualization, given in Fig. 5, shows the first four eigen modes for an 8x8 RVE for all volume fractions. Typically, the third and fourth modes are not considered, but are presented here for completeness. From the figure, it can be seen that the first mode pattern for ϑ_f=0.59 and 0.70 are identical, with the higher modes appearing only similar in nature. The first mode for ϑ_f=0.20,

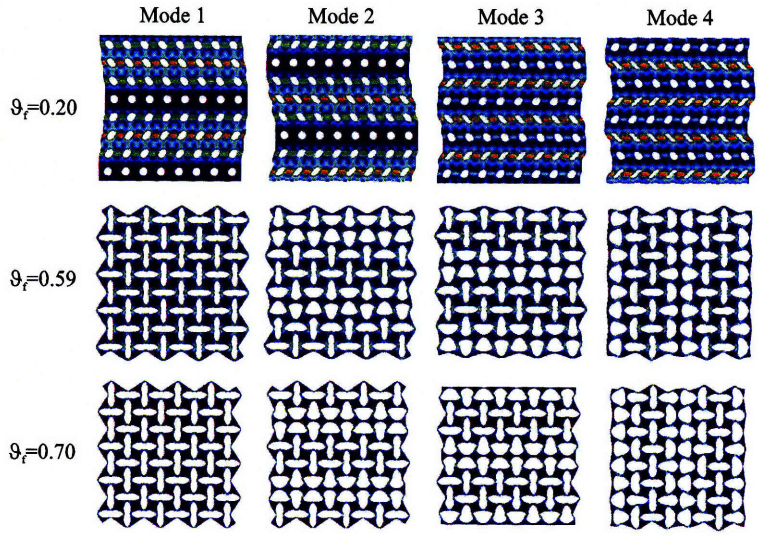

Figure 5: Eigen modes 1-4 for an 8x8 RVE of ϑ_f 0.20, 0.59, and 0.70.

unlike the other two, does not exhibit the alternating orthogonal ellipse pattern. Note also that each RVE is subject to the infinite periodic boundary conditions discussed in Section 2.1.2. Upon closer examination, it appears that volume fractions 0.59 and 0.70 give similar buckled results, while the loading of 0.20 differs. Figures 6-11 are thus given to further investigate this observation.

The first and second eigen modes for periodicity (RVE size) p_1=p_2=2, p_1=p_2=5, and p_1=p_2=6 [1] of ϑ_f 0.20 are given in Fig. 6. For the 2x2 case, mode 1 shows a shifted material mid-section with symmetry about the horizontal mid-plane. Although there is little void area change, there appears to be high stress concentration between the voids. Mode 2 differs in that it shows alternating

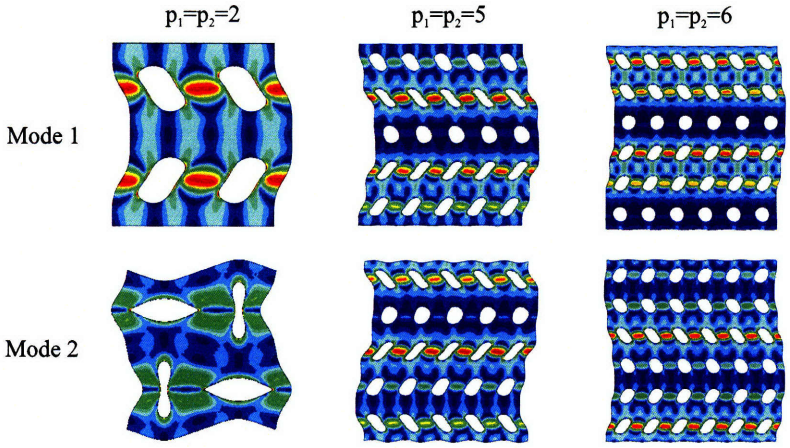

Figure 6: Eigen modes 1 and 2 for periodicity p_1=p_2=2, p_1=p_2=5, and p_1=p_2=6 for void volume fraction 0.20. There is no repeating pattern for the same mode in moving to higher periodicity, suggesting that these patterns are global changes which are unique to RVE size. The patterns are not from local ligament instability but are stable deformations from uniaxial compression.

orthogonal shapes with considerable area change. Due to the deformation pattern, this mode does not possess the horizontal symmetry of the first. The first mode of size 5x5 is interesting in that the extreme top and bottom rows follow the pattern displayed in the first mode of the 2x2. Furthermore, the stress levels and gradients between voids seems to be similar among the two sizes. The most important information conveyed by the figure, however, is that neither the 5x5 nor 6x6 RVE sizes can be created using 2x2 base units. This suggests that the patterns seen in the 2x2 and 6x6 are not periodic, but are global configurations unique to that specific size. Thus, the transformations seen are not a result of local buckling instability which give rise to global, periodic patterns, but are unique and stable deformations which would result from uniaxial compression [3].

Unlike unique global patterns of volume fraction 0.20, those of ϑ_f 0.59 show repeating configurations for even periodicity as RVE size increases. In other words, the larger sizes (e.g. 6x6) show sub-

[1] The symbol p_1 represents void number in the 1 or horizontal direction while p_2 captures void number in the 2 or vertical direction.

section patterns which are identical to those of the smaller sizes (e.g. 2x2); Fig. 7 makes this observation clear. The alternating orthogonal ellipse pattern for the first mode of the 2x2 is repeated throughout the mode 1, 6x6 representation. In fact, the 6x6 results can be duplicated

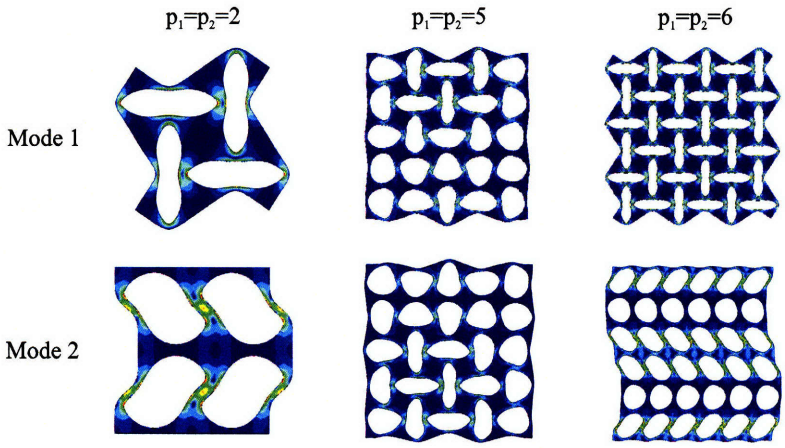

Figure 7: Eigen modes 1 and 2 for p_1=p_2=2, p_1=p_2=5, p_1=p_2=6 for void volume fraction 0.59. Unlike ϑ_f=0.20, there is pattern recognition within the first mode, namely the alternating orthogonal ellipse pattern for p_1=p_2=2 and p_1=p_2=6.

by creating a 3x3 matrix assembled using 2x2 units. This behavior suggests a regular, repeating pattern throughout even-sized RVEs as opposed to global pattern extending across all dimensions of the specimen. The alternating elliptical pattern does not exist for odd-sized RVEs, however. These configurations are not able to "select" or assume the elliptical pattern. The figure shows that the 5x5 lacks the repeating patterns of the 2x2 and 6x6. The relationship does not hold for mode 2 sizes either. Thus, the alternating orthogonal elliptical pattern is seen only in mode 1, even-sized RVEs. Interestingly, for RVE size 2x2, the mode 1 ϑ_f=0.59 (Fig. 7) shape resembles the ϑ_f=0.20 mode 2 shape (Fig. 6), while the mode 1 pattern of ϑ_f=0.20 is similar to mode 2 for ϑ_f=0.59.

The mode shapes resulting for ϑ_f=0.70 (Fig. 8) are very similar to those of ϑ_f=0.59. The alternating ellipse pattern for mode 1, even-sized RVEs is present with the p_1=p_2=6 size as a two dimensional construction of 2x2 units. Furthermore, the 2x2 mode 2 shapes are quite similar in pattern, with the voids of Fig. 7 appearing with additional skew. Differences include the dissimilar modes of p_1=p_2=5, mode 1 and p_1=p_2=5 and p_1=p_2=6 for mode 2. One subtle discrepancy

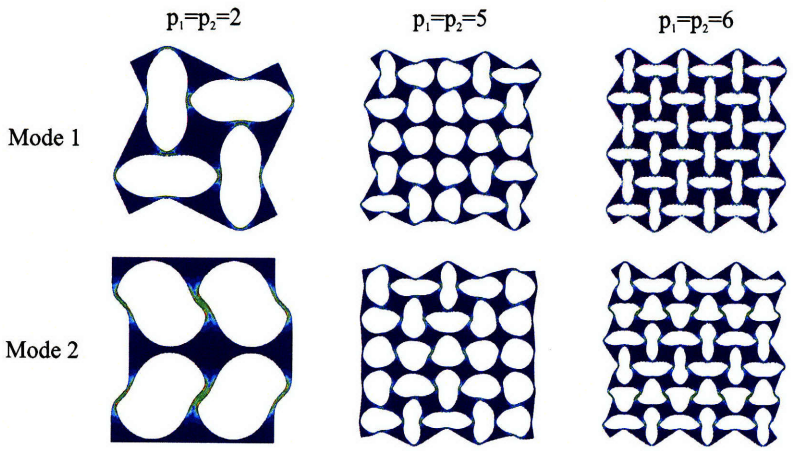

Figure 8: Eigen modes 1 and 2 for p_1=p_2=2, p_1=p_2=5, p_1=p_2=6 for void volume fraction 0.70. These results are very similar to those of ϑ_f=0.59–even periodicity pattern repetition among the first mode, similar 2x2 second mode–yet differ in p_1=p_2=5 for mode 1 and p_1=p_2=5 and p_1=p_2=6 for mode 2.

between the 0.59 and 0.70 cases is found in orientation of the elliptical pattern: The configurations of Fig. 8 are 180 degree rotations about the vertical mid-plane axis.

To capture the qualitative information displayed in Figs. 6-8, plots of nominal buckling stress (eigen value) against RVE size were constructed. Again, the results for ϑ_f=0.20 differ from the compatible 0.59-0.70 relationship. The pattern shown in Fig. 9 is unlike those given in Figs. 10 and 11 for ϑ_f= 0.59 and 0.70, respectively. The figure shows that the critical buckling stresses for the first two modes are virtually on top of one another from RVE size 3x3 up to 8x8. This means that the elastomeric array could assume either mode at nearly the same applied stress, depending on the boundary conditions and state of the system. In reality, the points appear in this manner because the structure is not buckling at all, but is following the same stable load path for each mode. Thus, the plot gives further support that the 0.20 specimens do not experience buckling; this behavior is suppressed due to the stability of the ligaments, which are thicker for the lower volume fraction. The buckling analysis rendered points in Fig. 9 for most of the RVE sizes, but failed for mode 1 and 2 for RVE size 9x9 and mode 1 for RVE=10x10. In both cases, the larger RVE sizes probably contributed to analysis breakdown.

The buckling stress-RVE trend for ϑ_f 0.59 plots much differently; Fig. 10 shows the results.

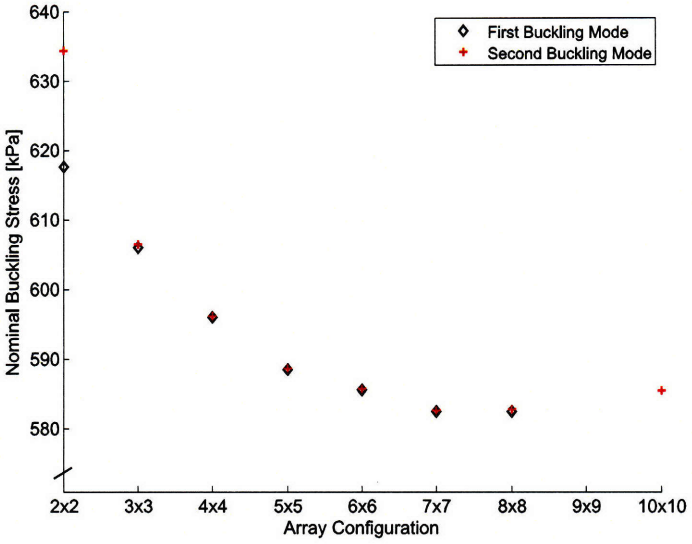

Figure 9: Critical buckling stress (eigen values) plotted against RVE size for void volume fraction 0.20. First and second modes for sizes 3x3 up to 8x8 appear almost on top of one another–a sign that buckling would not occur. Data for RVE size 9x9 and 10x10 do not appear since the "buckling" analysis failed for these conditions.

Immediately, it is clear that the overall patterns for Figs. 9 and 10 do not resemble each other. For volume fraction 0.59, the first mode points trace out adjacent, descending peaks in which the odd sizes make the peaks and the even sizes, the valleys. Of particular importance is the repeatable and lower value at which the even-sized RVEs buckle. Whether loading a 2x2 or 10x10, buckling will occur upon reaching about 26 kPa. As before, this suggests that the alternating ellipse pattern appearing in the 2x2 is repeating throughout all even sized array configurations. In the larger even sizes (4x4, 6x6, 8x8, 10x10), complete buckling occurs once the base unit (2x2) reaches the critical buckling stress. For odd sizes, first mode values occur in an almost linear decreasing fashion. Since there is no repeated sub-unit as in the even configurations, each critical stress value is different. The second mode trend approaches that of the first, but is in resemblance from size 6x6 onwards. Additionally, odd second mode values coincide with those of mode 1. Finally, note that the range of stress values is an order of magnitude lower than those of ϑ_f 0.20, owning to the fact that the structures are less stiff with less material, thus requiring a lower stress for buckling.

The plot of buckling stress vs. array configuration for ϑ_f=0.70 (Fig. 11) is nearly identical to that for volume fraction 0.59. Again, the figure shows a peak-like pattern with a nearly horizontal base

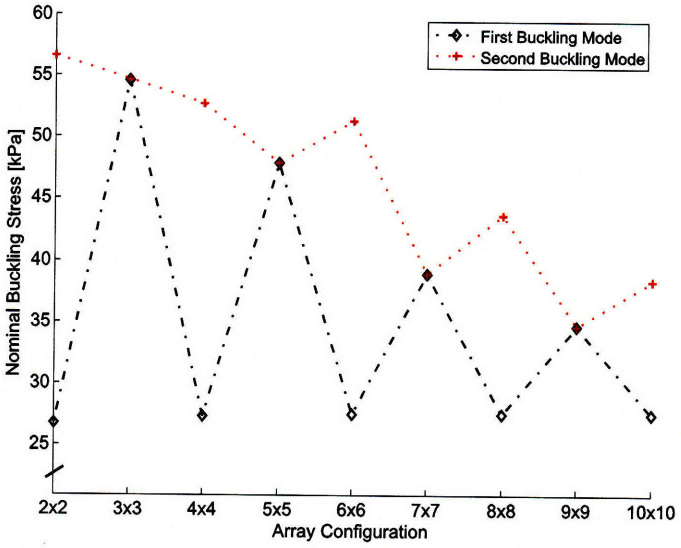

Figure 10: Nominal buckling stress vs. array configuration for void volume fraction 0.59. Critical first mode stress values for even array sizes occur at nearly the same level, while values for mode 1 and 2 odd sizes coincide.

and a linearly decreasing set of apex points; the first and second mode odd sized points also coincide. Additionally, the stress range has dropped another order of magnitude. Thus, the conveyance of the figure is that similar behavior occurs when volume fraction is increased and that this behavior occurs over a lower stress range. In comparing Figs. 10 and 11, there seems to be higher variability among even-sized mode 1 points for ϑ_f 0.70. The largest change for ϑ_f 0.59 is about 2%, occurring between RVE sizes 2x2 and 4x4; the largest variation in ϑ_f 0.70, however, is 10%, between sizes 8x8 and 10x10. Furthermore, variation among the other points of volume fraction 0.59 is well below 1% while volume fraction 0.70 shows another 6% and 8% variation. The point locations for volume fraction 0.70 may support alternate behavior as RVE size increases, but their variability is more likely due to analysis process. In any case, the variation is not large enough to invalidate the agreement in volume fraction behavior and thus the claim that increased volume fraction will yield pattern transformation at lower values of stress still holds. These results for eigen mode and value for varying RVEs indicates that"even" RVEs are capturing the actual lowest energy configuration; that this is indeed true has been confirmed using a Bloch wave analysis approach [3].

Supplementing the buckling stress-array configuration plots are stress-strain data, obtained using

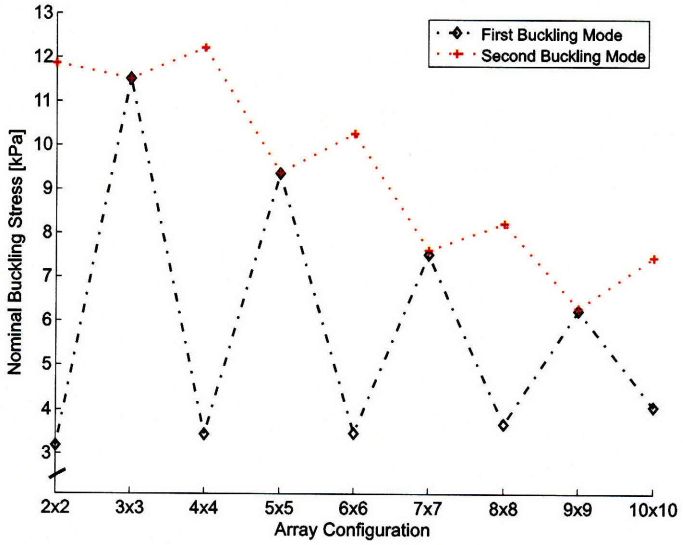

Figure 11: Critical buckling stress and array configuration for ϑ_f=0.70. Trends shown agree with those of Fig. 10 where first mode even-size values were nearly constant, first mode odd-size values were linearly decreasing, and first and second mode odd-size values were coincident.

the imperfection-perturbation technique. A 2x2 specimen for volume fractions 0.59 and 0.70 was loaded to 10% strain, while a ϑ_f 0.20 2x2 was loaded to 20%. Results are shown in Figs. 12-14. Because the ϑ_f=0.20 specimens did not undergo buckling, the stress range shown in Fig. 12 is much higher than that of Fig. 13; hence separate plots.

The loading of the ϑ_f=0.20 specimen was a stable process with no pattern transformation–it was simply uniaxial compression. The stress-strain behavior (Fig. 12) shows linearity at small strain, but increases in stress rapidly when strained beyond 10%. The stress values required for deformation are also relatively large, nearly reaching 1 MPa at 20% strain. Overall, the stress-strain behavior of the ϑ_f=0.20 specimen was similar to that of a non-voided specimen. Visualization of the 2x2 structure during certain stages of loading are shown in Fig. 14. Throughout straining to 10%, the structure compresses in the vertical direction and expands horizontally due to the Poisson effect. The circular voids do not assemble into the alternating orthogonal pattern, but simply elongate along their horizontal axes and compress along their vertical ones.

The stress-strain curves in Fig. 13 for ϑ_f=0.59 and 0.70 are quite distinguished from that of volume fraction 0.20. Instead of an increasing slope, these volume fractions behave such that initial linearity

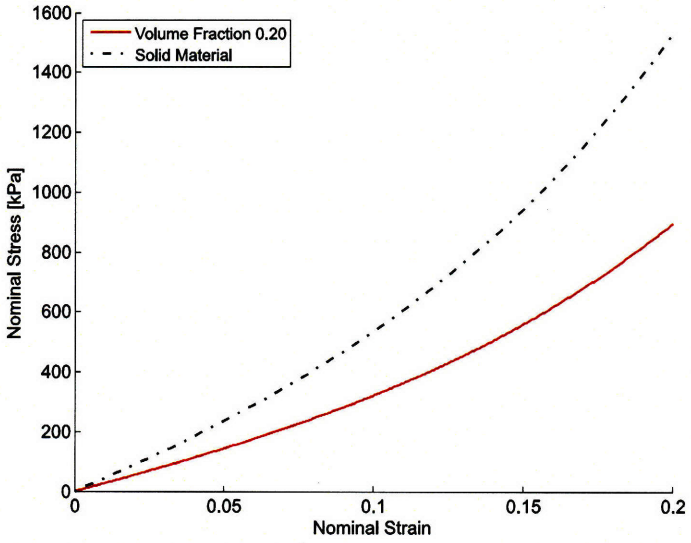

Figure 12: A non-linear stress-strain curve for ϑ_f=0.20. Loading of this specimen was a non-buckling process and was thus a simple compression. Note that stress levels are much higher than those of Fig. 13 where buckling did occur. Also included is a stress-strain curve for an unaltered piece of material.

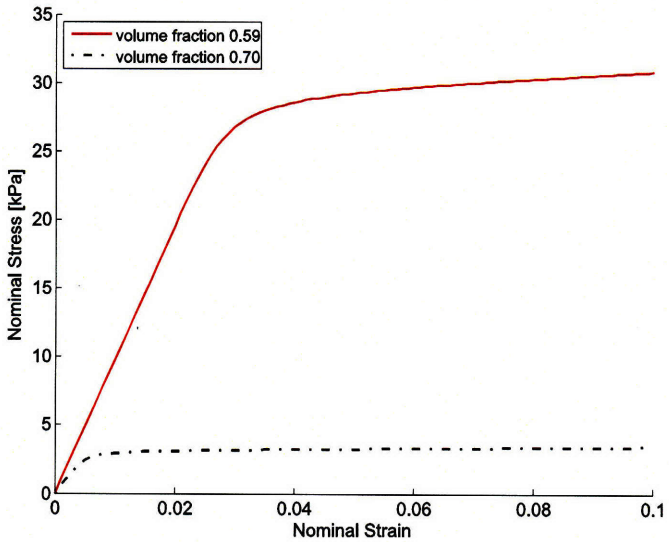

Figure 13: Stress-strain plot for ϑ_f= 0.59 and 0.70 showing initial linearity, departure near the critical buckling stress, and large-strain leveling.

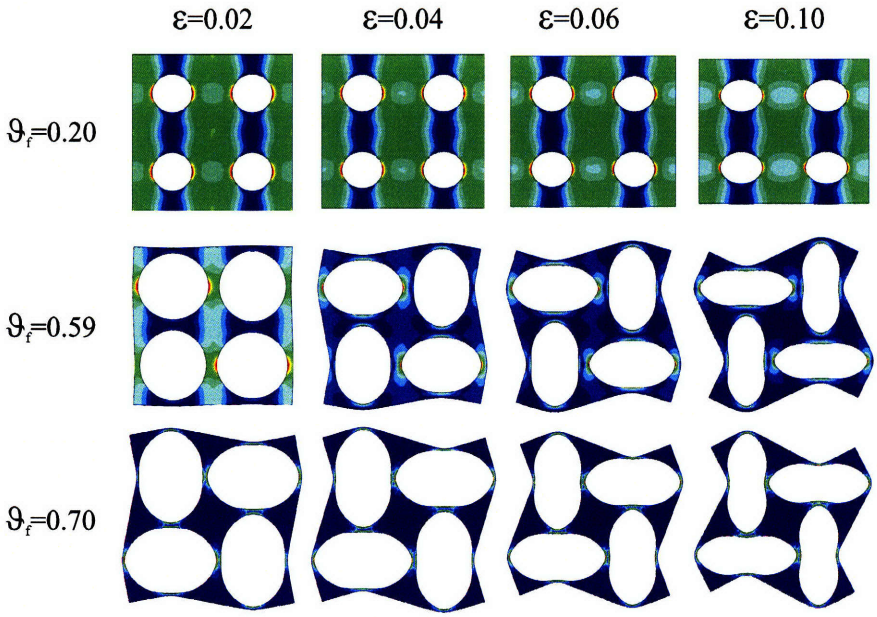

Figure 14: Visualization of strain progression capturing the compressive loading of ϑ_f=0.20 and buckling of ϑ_f= 0.59 and 0.70. Pattern transformation occurs more rapidly and at lower stress levels for volume fraction 0.70 since there is less material present.

rounds off to a horizontal slope. The linear regime of the curves corresponds to loading prior to buckling while the transition region signals buckling onset. This is in agreement with other figures presented. In Fig. 10 (critical buckling stress vs. RVE size for ϑ_f 0.59) the first mode critical buckling stress for a 2x2 array occurs at about 26 kPa which is about where the stress strain plot (Fig. 13) departs from linearity. Continuing, Fig. 14 shows the buckling transformation occurring between 2% and 4% strain which is the region of transition in Fig. 13. The same verification can be made for ϑ_f=0.70 using Figs. 11, 13, and 14.

After studying the loading behavior of 2D specimens of varying volume fraction and RVE size, it can be concluded that alternating orthogonal elliptical pattern transformation occurs for even-sized structures of ϑ_f 0.59 and 0.70. Furthermore, the critical buckling stress for these specimens is independent of size, occurring at nearly the same value within a given volume fraction group. It has also been discovered that increasing the volume fraction to 0.70 brings buckling at lower values of stress and strain due to the smaller amount of material present. Finally, it has been determined that specimens of volume fraction 0.20 do not exhibit microstructural instability, but

undergo stable compression upon loading.

3.2 3D Periodic Structures of Varying Void-Volume Fraction

To study the effect of a third dimension on transformation behavior, an analysis was conducted on 3D structures of varying volume fraction. Since specimens of ϑ_f 0.20 failed to buckle in two dimensions, this volume fraction was not examined further. The number of RVE sizes considered was also reduced since the larger configurations (7x7 through 10x10) were computationally intensive and unnecessary for showing the continuation of the repeating elliptical pattern. It was found that transformation characteristics for the 3D structures were in good agreement with those of the 2D specimens.

The results of the eigen analysis were the first to show such excellent agreement, as the buckling behavior was essentially the same as for the 2D results. Figures 15 and 16 show this agreement qualitatively. For 3D structures of volume fraction 0.59 and 0.70, even-sized RVEs assume the alternating orthogonal ellipse pattern for the first mode shape. As before, Fig. 15 shows that the larger 6x6 size can be constructed using 2x2 base units. This construction would be possible, but to exactly replicate the 6x6 as shown, the 2x2 would have to be rotated by 180 degrees about its horizontal axis. Such a required alteration does not jeopardize the relationship between these two sizes, however. Both structures could have been theoretically cut from the same infinite, periodic sheet, differing only in horizontal or vertical offset of one column or row. On a separate note, the presence of a repeating pattern in the 6x6 size is evidence for a periodic transformation instead of a unique global change; this conclusion was drawn in 2D as well. Finally, the 5x5 is unable to render the elliptical pattern since its matrix is of odd dimensions. The buckling outcome for volume fraction 0.70 (Fig. 16) is nearly identical. Among the 6x6 ellipse pattern is the 2x2 mode 1 shape. As in the case of ϑ_f 0.59, the 2x2 and 6x6 patterns are offset by one layer of voids. After a one-half revolution rotation about the horizontal axis, the 2x2 would match perfectly when overlayed upon the 6x6 structure.

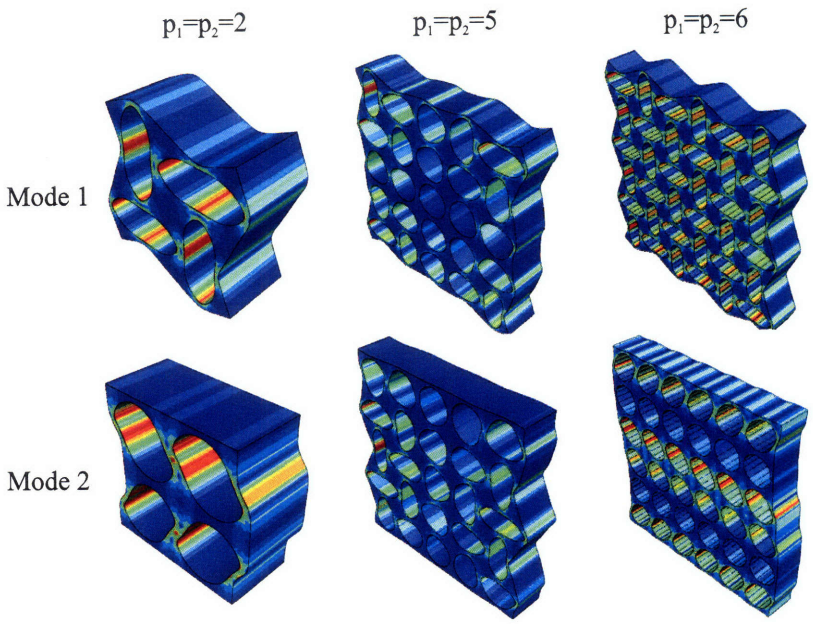

Figure 15: The 3D eigen analysis for ϑ_f 0.59 shows buckling results that are very similar to those of two-dimensions: The even-sized RVEs show the alternating orthogonal ellipse pattern in their first mode while the odd-sized RVE in unable to capture this transformation pattern.

Unlike the findings of Figs. 15 and 16, the buckling stress vs. array configuration plots for the 3D structures may indicate that adding a third dimension has some effect on transformation outcome. Figure 17 shows critical buckling stress plotted against array size for volume fraction 0.59; Fig. 18 shows the same for fraction 0.70. Both figures show much greater variation in their even-sized mode 1 points than was shown in 2D. Volume fraction 0.59 shows a 5% then 10% jump between successive points while buckling stress increases by 30% between the first and second even-sized mode 1 points for volume fraction 0.70. Additionally, ϑ_f 0.59 is now showing the "lifting" trend that was shown for volume fraction 0.70 in 2D. However, the maximum variation in 3D for ϑ_f 0.59 is about the same as that for ϑ_f 0.70 in 2D. If the 2D variability was associated with analysis process, then this similarity would suggest that moving to three dimensions does not affect transformation outcome. But this justification does not apply to the drastic change in buckling stress from 2x2 to 4x4 for volume fraction 0.70. Even though the stress values are low in this case, the change in moving between the points is still about 30%. Furthermore, the second and third even-sized mode 1 points have nearly the same stress value, eliminating any possibility of systematic variability. Thus there is a chance that there may be something unexpected happening for the 3D 2x2 of volume fraction

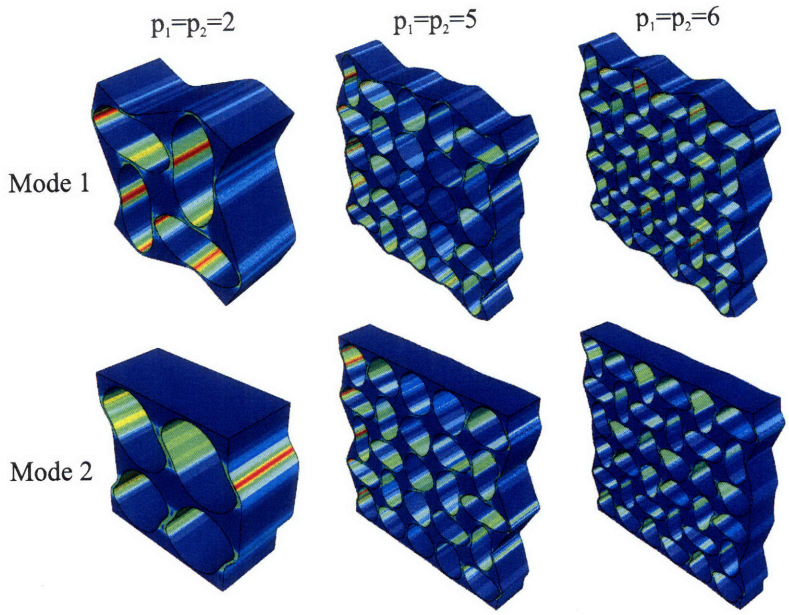

Figure 16: Buckling for volume fraction 0.70 is very similar to that of ϑ_f 0.59; the same trends are seen: An alternating, orthogonal elliptical pattern for the even-sized structures with an inability of the odd-size to show this pattern.

0.70–the second mode trend can be used to evaluate this claim. In the 2D plot of eigen value vs. RVE size (Fig. 11), the mode 2 saw-tooth pattern begins at size 3x3 with the 2x2 stress value lying above that of the 3x3. In the 3D plot (Fig. 18) however, the saw-tooth behavior commences with the 4x4 and the 2x2 stress value falls below that of the 3x3. The fact that both mode trajectories appear differently between the 2D and 3D specimens for the 2x2 of volume fraction 0.70 may be evidence that alternate transformation behavior might be occurring. If the top surface of the 3D 2x2 was not constrained, alternate results may have been realized. It may be valuable to investigate this matter further to determine whether constraining the top surface actually has any effect on the transformation outcome.

Although there is uncertainty associated with the 3D buckling stress-array configuration plots, they provide important information about 3D pattern transformation. As in the corresponding 2D plots, these figures show the important mode 1 saw-tooth pattern. Despite their variability, the even-sized mode 1 points continue to fall roughly along a horizontal line. This suggests that the buckling of the larger-sized RVEs is occurring in the same manner as in the smaller sizes. The relatively larger

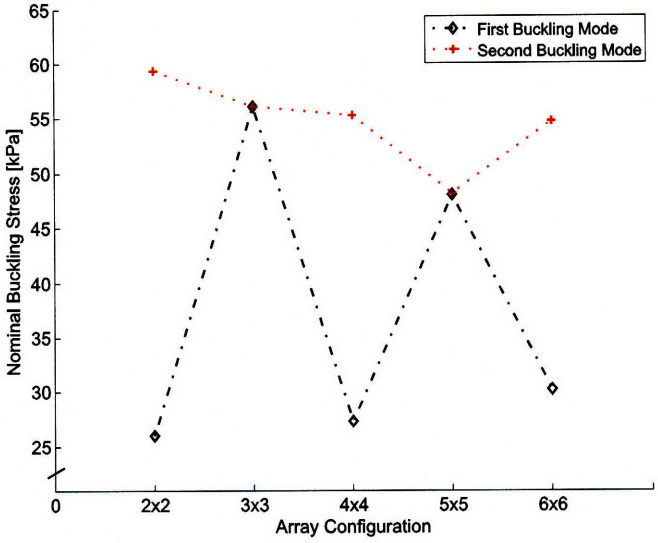

Figure 17: Critical buckling stress vs. RVE size for three-dimensional structures of volume fraction 0.59. The mode 1 saw-tooth pattern is familiar–it was seen in the corresponding 2D plot. Also important is the closeness of the even-sized mode 1 buckling stress values, suggesting that buckling in the larger-sized RVEs occurs in a similar manner to that in smaller sizes. The even-sized mode 1 "lift" seen in the 2D ϑ_f 0.70 plot is evident here.

required stress to buckle the odd sized configurations indicates that they are unable to capture the even-sized first mode. Despite the variability of Figs. 17 and 18, they allow familiar conclusions to be drawn.

The stress-strain curves for the 3D structures also show trends that were seen in 2D. Figure 19 gives the stress-strain behavior for 3D structures of both volume fractions. As before, the figure shows an initial linear region giving way to a transition region before the curves finally level off. It also shows that volume fraction 0.70 transitions more rapidly (i.e. at smaller strain) and at lower stress values. The agreement in the linear slopes is also expected since the modulus describes material behavior, of which they are the same. Additionally, the regions of change for each curve are in agreement with their respective 2D counterparts (which are shown in Fig. 13). In Fig. 19, volume fraction 0.59 begins its buckling transition at about 33 kPa while ϑ_f 0.70 begins at about 4 kPa. In 2D, ϑ_f 0.59 starts at around 28 kPa while 0.70 begins at about 3 kPa. The strain values at transition are also in agreement, with ϑ_f 0.59 at 5% in 3D, and 3% in 2D and ϑ_f 0.70 at 1% in 3D and slightly less than 1% in 2D. The similar stress-strain response between 2D and 3D analyses is reassuring

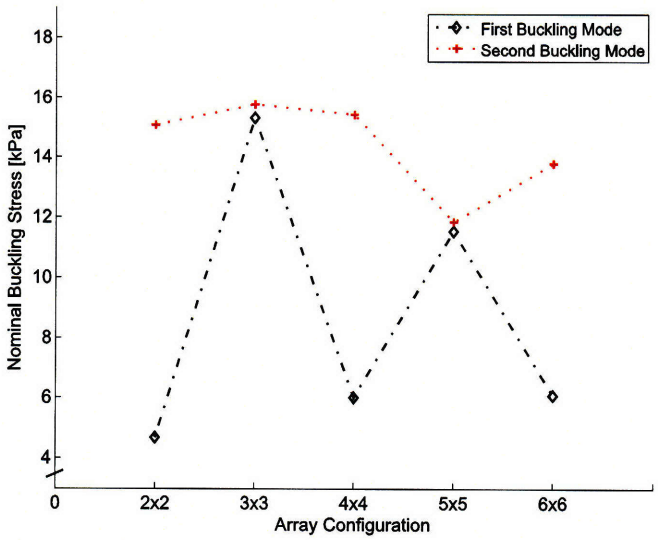

Figure 18: Eigen value plotted against array configuration for 3D structures of volume fraction 0.70. The important saw-tooth shape is overshadowed by the large jump in stress value in moving from the 2x2 to 4x4 along the mode 1 path. The mode 2 pattern also differs from that seen for the same volume fraction in two-dimensions.

and validates the imperfection-perturbation technique used to obtain the plots. It does not help describe the variance in the buckling stress-array configuration plots, however, since a different analysis (eigen analysis) was used to produce them. One final note: As seen in two-dimensions, the "steady-state" slope (i.e. the slope after full transformation) for volume fraction 0.59 appears as non-zero while that of ϑ_f 0.70 seems horizontal. This difference is primarily due to volume fraction as the 0.59 requires slowly increasing levels of stress for further strain after transformation since it possesses greater structural stiffness.

The findings for three-dimensional structures of ϑ_f 0.59 and 0.70 were largely in agreement with those in 2D. The alternating orthogonal ellipse pattern was repeated for even-sized RVEs of both volume fractions, the critical stress values for these configurations fell on a nearly horizontal line, and the higher volume fraction buckled at lower stress and strain values. Specifically, the mode shape figures showed that there was very little qualitative difference in moving to three dimensions, while the stress strain plots displayed the non-zero post-transformation slope for volume fraction 0.59. Larger variation among even-sized mode 1 points on the buckling stress-array configuration plots was also noted. In particular, the 2x2 size of ϑ_f 0.70 showed variations which might be worthy

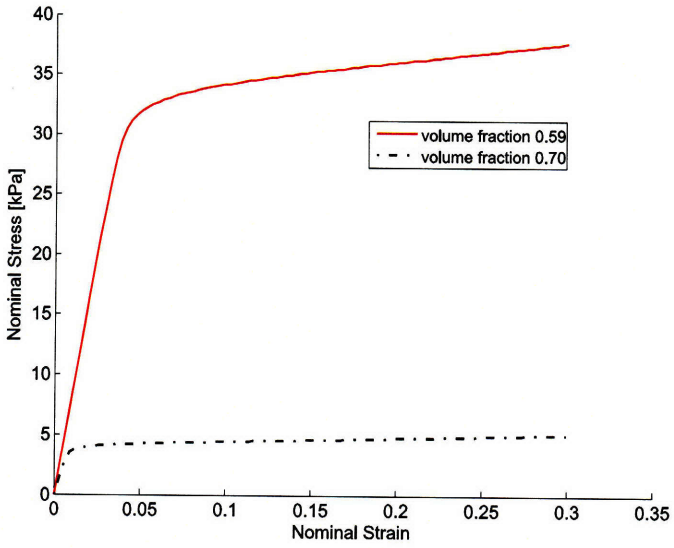

Figure 19: Stress-strain behavior for 3D structures of volume fraction 0.59 and 0.70. As in the 2D case, transformation is seen earlier and with lower stress values in the higher volume fraction specimen. Note the agreement in initial slope for the volume fractions and the non-zero post-transformation slope for volume fraction 0.59.

of further investigation.

3.3 3D Periodic Structures with Thin-Film Coating

Once the behavior of the three-dimensional structures was understood, it was desired to further the analysis by adding a thin-film layer to one of the free surfaces of the 3D structure. The layer was 0.5 mm thick and was placed on specimens of ϑ_f 0.59 and 0.70 and RVE sizes 2x2, 3x3, and 4x4 [2]. It was predicted that pattern transformation would occur as usual in the 3D structure while the film would move out-of-plane in some corresponding manner. Indeed, it was found that each size for all volume fractions showed such film motion upon deformation. Additionally, an interesting film-induced, large-strain channel pattern was discovered. On the other hand, some results encountered were unexpected. As examples: The stress-strain curve appeared much differently than it did without the film, also, sharp corners were seen on the endpoints of the major axis for the horizontal ellipses.

[2]The RVE sizes 3x3 and 4x4 were used in place of 5x5 and 6x6 (respectively) due to limitations in computing power required for the larger sizes.

Loaded structures with film are shown at 4% strain in Fig. 20 (ϑ_f 0.59) and Fig. 21 (ϑ_f 0.70). Apart from the presence of the film, one difference from simple 3D loading is that the top (film) surface can no longer be constrained. This influenced the method of analysis: Instead of using *BUCKLE, the perturbation technique was used to visualize transformed results. This method only gave results up to 4% strain for size 3x3 since its deformation was not approaching a buckling mode and the numerical method of ABAQUS was diverging for this case. Therefore, the rest of the specimens were presented at 4% for comparison. The patterns appearing in each figure are

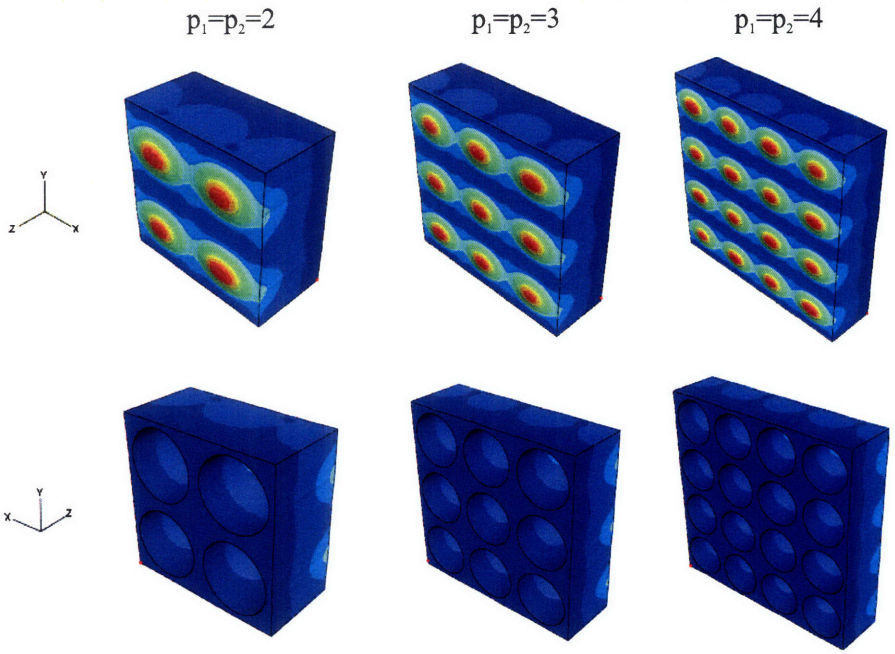

Figure 20: Three-dimensional periodic structures of volume fraction 0.59 with film at 4% strain viewing front (top row) and back (bottom row) surfaces. Although elliptical pattern transformation has not yet commenced, film activity can be seen. Specifically, domes have begun to form over the voids while horizontal "channels" are present between dome rows.

nearly identical, the only difference being the degree of nodal displacements within the structure. The front views show that the sections of film which fall over the voids appear as convex domes which are beginning to rise out of the film plane; the back-side views give no hint of structural pattern transformation. This is interesting–especially in the 0.70 case–because the structure would have been buckled at this level of strain without the presence of the film (refer to Fig. 19). Thus, the film seems to be suppressing transformation, or at least delaying it for further strain. (This

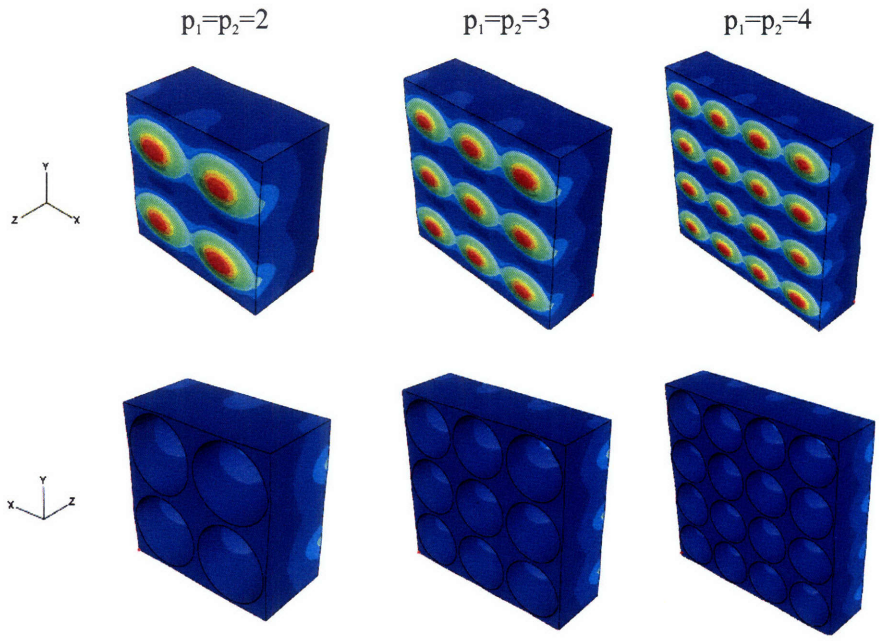

Figure 21: Loading results at 4% strain for periodic structures (of volume fraction 0.70) with film. These visualizations appear as nearly identical with respect to those for ϑ_f 0.59, shown above.

behavior can be seen more clearly in the stress-strain curve (Fig. 24) which will be presented later in this section.) Since the figures give visualizations at relatively small strain, conclusions about pattern transformation for the various sizes cannot be made. They are helpful, however, in showing the presence of a dome array pattern and horizontal "channels" formed between dome rows. These film transformations could prove useful in practical applications for these structures.

In studying structure-film behavior with further deformation, 2x2 structures of both volume fractions were considered to 10% strain. Contour maps of the x-y plane (coordinate systems shown in Figs. 22 and 26) and various material cross sections are shown (Figs. 22 and 23) for more detailed examination. The contour map given in Fig. 22, for example, is a color based representation for displacement in the z-direction; dark blue is negative displacement (into the page) while red gives maximum positive displacement (out of the page). Also included in the figure are cuts taken through the material. The slices follow the path of the dashed line of their corresponding numbers. These numbers also orient the line, i.e., they indicate which endpoint is start. Regarding results, the figure shows little activity for a strain of 1%. There is some slight positive film displacement in

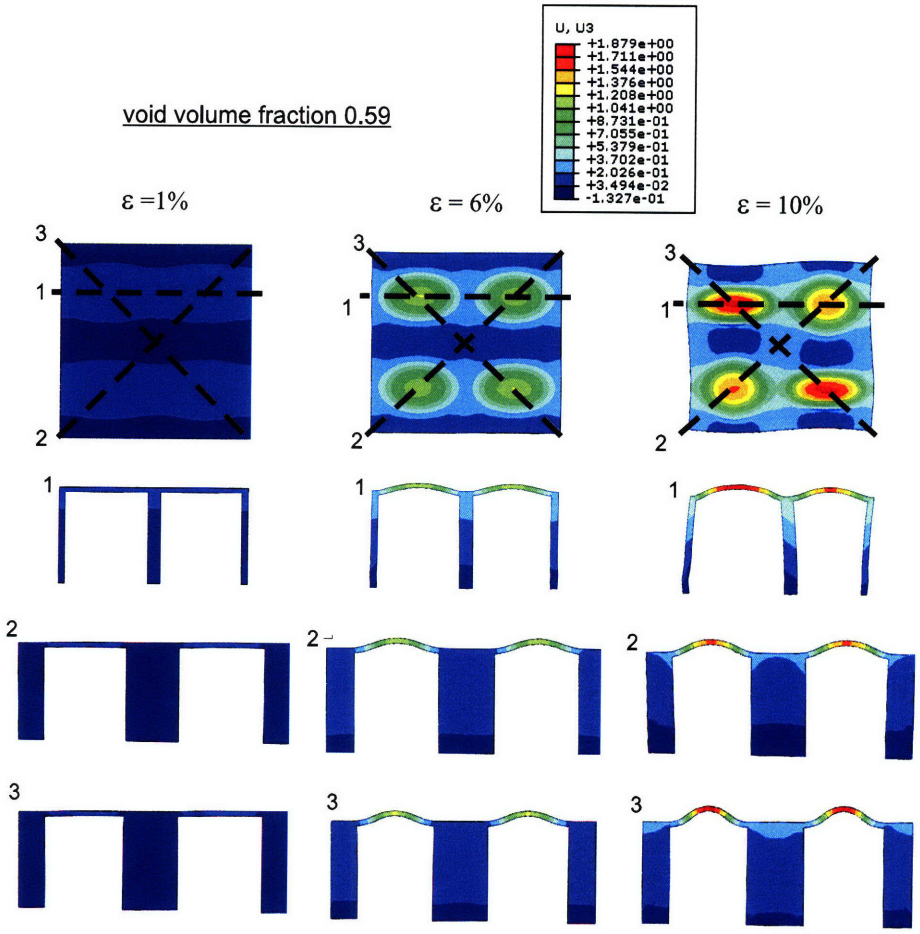

Figure 22: Contour maps of z-axis displacement shown with sectional slices along three paths for structures of volume fraction 0.59. As strain progresses, development of a horizontal channel between void rows as well as considerable film displacement appear.

the vicinity of the voids and the horizontal channel is beginning to develop. The cuts offer no further information only granting support for the lack of film or structure displacement. Much greater displacement occurs for 6% strain, however. The domes are displaced a considerable amount (about 1 mm, or twice the film thickness) and the channel is now starting to present itself. It is formed because the inter-void surface remains planted while the film around the voids grows out of the plane, creating sides for the channel. Shape change for the circular voids is also evident as the once circles are becoming more elliptical. In looking at the first cut, the middle valley is not as deep due to elongation of the structural ligament (shown in light blue). In contrast, the central area between the domes in the second cut remains near its datum, creating a flatter and lower valley. Differences

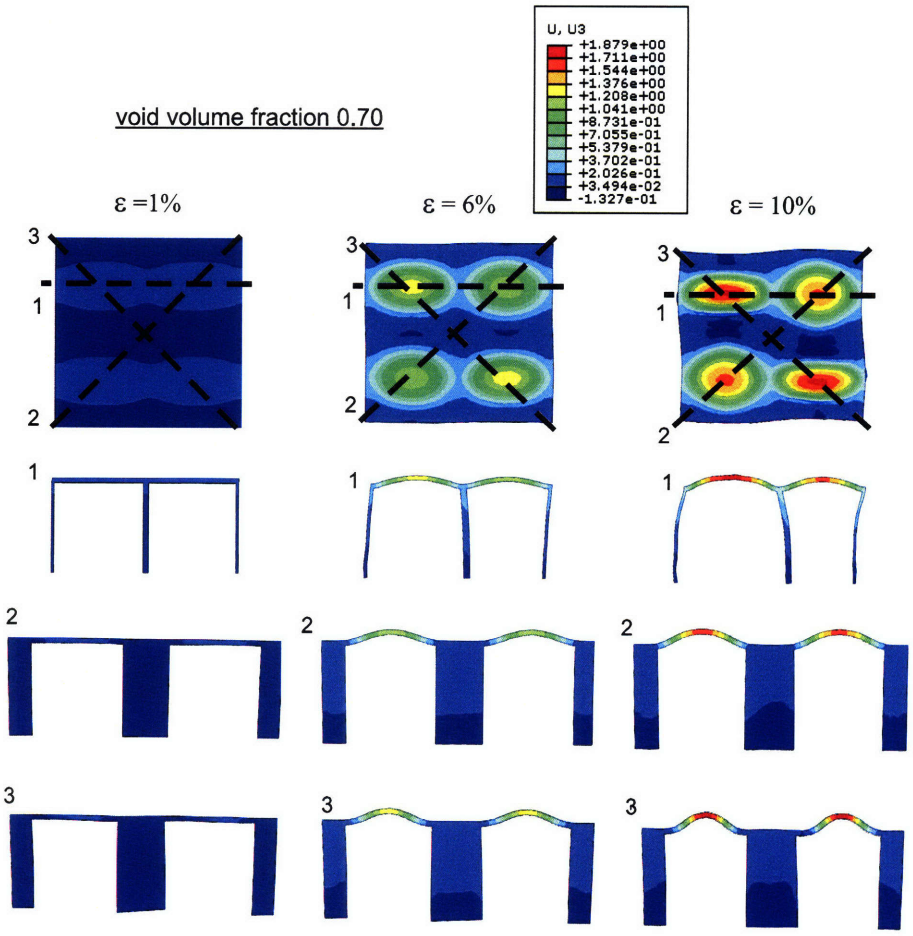

Figure 23: Contour maps and sectional cuts for ϑ_f 0.70. Here the results are very similar to those of Fig. 22 but show the differences associated with having less material in the underlying structure.

in vertical gradient are also seen in comparing cuts 1 and 2: Cut number 1 shows more vertical displacement in the structure than is shown in cut 2. The outcome is that the void sections parallel to the x-axis are raised higher than the central portion, giving rise to the horizontal channel. A similar mechanism is observed for the third cut, but here there is slightly larger displacement at the node peaks (shown as small yellow dots).

The larger displacement of the node peaks along cut 3 (relative to cuts 1 and 2) is further accentuated as strain increases to 10%. A greater area of each third cut dome is at a displacement of nearly 2 mm (shown in red). This is caused by the underlying pattern transformation. Those domes which lie above the horizontally oriented ellipses experience larger displacements while those over

the vertically oriented ellipses experience smaller ones. Note that the effect is reciprocated: The film acts on the structure to create more slender horizontal ellipses and nearly circular "vertical" ones. With 10% strain, the channel is developed still further, showing an in-plane bend and two troughs (each shown in dark blue). Cut 1 shows considerable z-axis displacement as well as the non-straight upright pieces. The second cut shows a stretching of the section towards the top and along its horizontal axis. Finally, the third cut highlights the substantial height (nearly 2 mm) attained by the dome peaks. It also shows that the upright posts are much straighter than those of cut 2.

Figure 23 gives contour maps and sectional cuts for ϑ_f 0.70–results are very similar to those of Fig. 23. At 1% strain, the contour map shows a hint of channel formation while the cuts indicate that little sectional displacement is occurring. Cut 3, however, shows that there is some slight horizontal stretching of the upper portion of the section which was not seen at 1% in ϑ_f 0.59. At 6%, the contour map shows a similar displacement field (with respect to 6% strain at ϑ_f 0.59) but shows more yellow on the domes along the third cut. The first cut at this strain level shows the further motion of the upright pieces due to their slenderness. Again, the third cut shows increased stretching across the upper portion of the slice. For 10% strain, the increased motion of the uprights is seen and the channel becomes more level across the bottom as opposed to having two distinct troughs. In combination with Fig. 22, Fig. 23 shows that even at moderate strains, the film exhibits interesting behavior.

The levels of strain at which the contour maps and sectional cuts were taken are marked on the stress-strain plot of Fig. 24. It is understandable that both volume fractions show little motion at 1% because they are still in their linear regime, long before transformation. By 6% strain, it is clear that there is a significant disparity in stress level between volume fractions 0.59 and 0.70. At this point, it seems that the specimen of ϑ_f 0.70 is into its transformation regime while that of ϑ_f 0.59 remains in the linear region. This observation explains the motion of the uprights along cut 1 in Figs. 22 and 23. For volume fraction 0.59, the uprights are relatively vertical because pattern transformation has not occurred yet. For ϑ_f 0.70, however, the uprights are displaced because

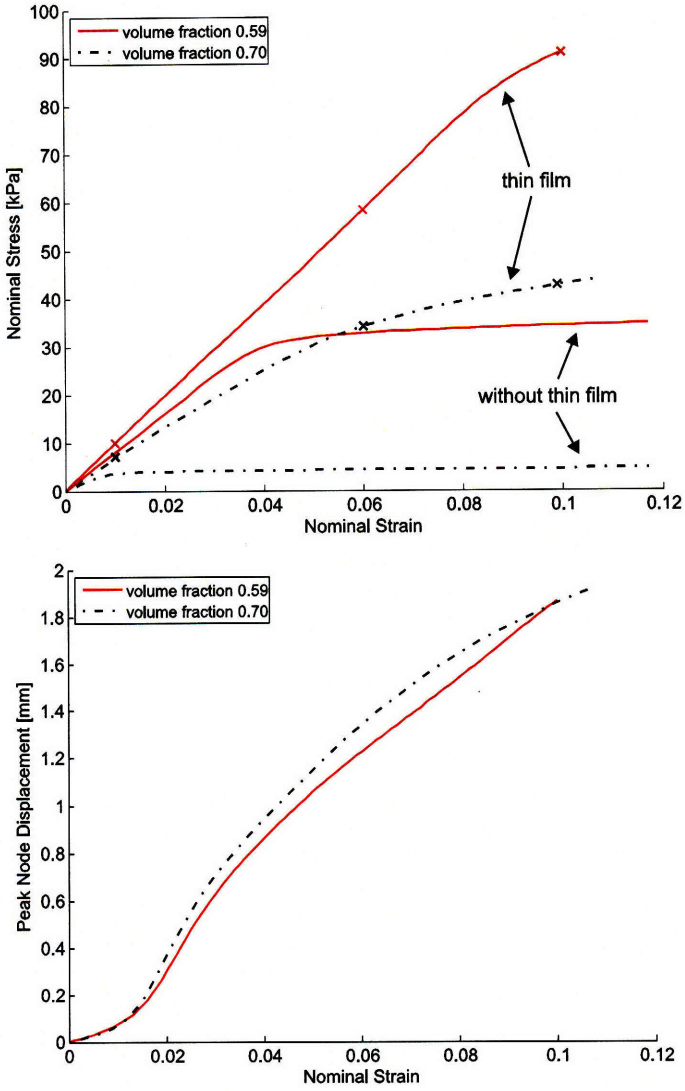

Figure 24: Stress-strain plot with graph of peak node displacement vs. strain for each volume fraction. The stress-strain plot give marks indicating the strain levels used for contour maps and sectional cuts. It shows that pattern transformation is prolonged and postponed due to the presence of the film. The peak node displacement plot, on the other hand, gives displacement in the z-direction for the peak of the top left dome as shown in Figs. 22 and 23. It shows different regions in which rate of height increase changes.

pattern transformation has taken place. Going further, the distance at the bottom between the leftmost and middle uprights is larger than between the middle and rightmost upright because it captures transformation of the horizontal ellipse, while the other distance measures the minor axis of the vertically oriented ellipse. By 10% strain, the 0.59 has transformed and the resulting motion of the vertical uprights of cut 1 is evident. Figure 24 also shows the differences in stress-strain behavior with and without the film coating. With no film, transformation occurs sharply and at lower strain; film presence results in a gradual transformation. Additionally, the points of transition–about 5% for ϑ_f 0.70 and 9% for ϑ_f 0.59–occur long after the 1% for 0.70 and 5% for 0.59 when no film is present. Thus the presence of the film postpones transformation and also prolongs the process.

Also included in Fig. 24 is a plot of dome-peak displacement vs. strain. The specific node trajectory plotted is that located at the apex of the top left dome (as shown in Figs. 22 and 23) for each volume fraction. It is shown along with the stress-strain plot so that peak node behavior can be easily examined in the context of the global structure. Before 1%, peak node displacement seems to be linear with strain, but just before 2%, the rate of height displacement increases rapidly for both volume fractions. Furthermore, there is an inflection point near this level of strain, meaning that rate of increase of height is at a local maximum. Beyond this point, the curve for volume fraction 0.59 falls below that of 0.70, which is expected and verifiable using the contour maps. Additionally, the rate of height increase seems to drop off after transformation. This can be seen best in ϑ_f 0.70 where the peak node slope begins decreasing further after about 5% strain, corresponding to the point of transformation. This cannot be seen for ϑ_f 0.59 because it does not transform until around 10% and the peak node data does not extend beyond this point. The peak node displacement plot shows that there are distinct regions for rate of height increase: The initial shallow slope transitions to an inflection point which leads to a region of decreasing slope after transformation.

The markers on the stress-strain plot are also helpful in examining the strain progression visualizations presented in Figs. 25 and 26. These figures mostly verify behavior that has already been discussed, but bring a new perspective so that additional characteristics can be recognized.

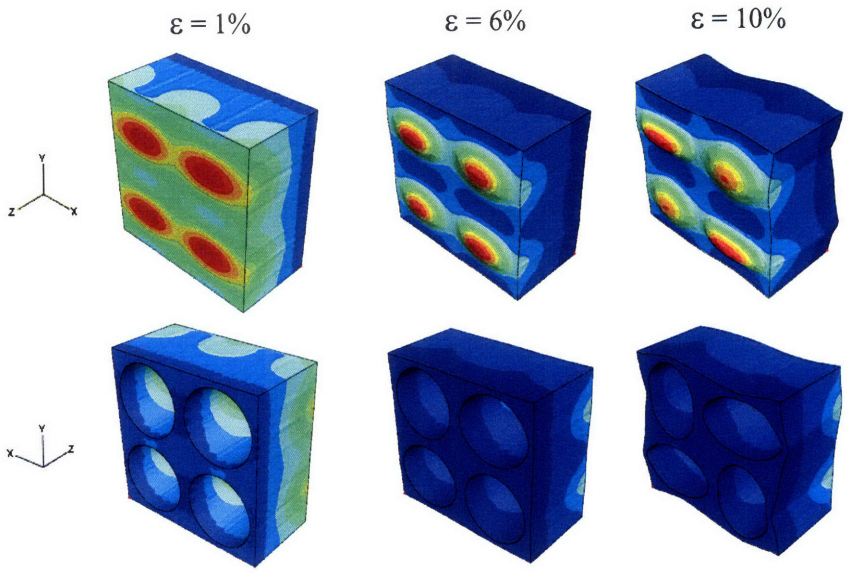

Figure 25: Visualizations showing strain progression for a 2x2 film structure of volume fraction 0.59. Through 6% strain, dome displacement is apparent while 10% strain is required to notice the z-axis variation and corners appearing at the ellipse edges.

Again, results for 1% strain are fairly uninteresting beyond the start of domes displacement. By 6% though, film motion is drastic. In the three-dimensional views of Fig. 25, the central channel can be better visualized and the dome shapes can be better compared. At this point, they are hardly indistinguishable, but at 10% strain, it is clear that the "cut 3" domes have elliptical shapes with larger displacement while the "cut 2" domes are more circular. On another note, the figure shows structural behavior that was not anticipated: There is variation along the z-axis and sharp corners at the edges of the ellipses. These two patterns are related since the lines of indentation which run along the z-axis are connected at the ellipse edges. The pattern changes are certainly brought on by the presence of the film and result due to the structure's asymmetry. Since the film-bonded edge is stiffer, it does not deform as much as the backside in the y-direction. This results in compression of the horizontal voids to the point where they become creased at the edges. This forces the surrounding structural material away and out of its plane, causing the z-axis variation. The influence upon the vertically oriented ellipses is to force the minor axis to a corner on its free edge. Similar behavior can be observed for ϑ_f 0.70 in Fig. 26; results here though appear more rapidly and with greater magnitude. In particular, the z-axis variation and ellipse corners are easily seen at

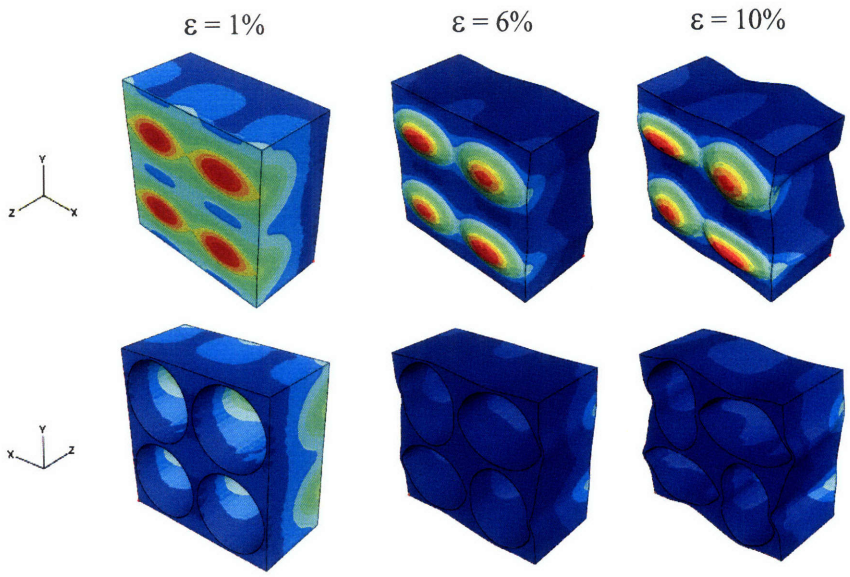

Figure 26: Strain progression for 2x2 film structures of volume fraction 0.70. The features here are similar to those of ϑ_f 0.59 but appear at lower strain and in a more pronounced manner.

6% strain. By 10% strain, these features are developed nearly to the point of making the structure unrecognizable. Unfortunately, film simulations for the larger RVEs would not run to this level of strain, so such interesting behavior could not be evaluated for these larger cases.

The presence of the film produced interesting results which varied from those of the non-film 3D structures. Upon structure loading, the film created a horizontal channel between void rows and also showed considerable out-of-plane displacement for the developed domes. It was discovered that displacement at the dome peaks increased at different rates depending upon the structure's strain level. The presence of the film also affected the stress-strain curve, making transformation more gradual and at larger strain. Finally, it is responsible for inducing unanticipated structural change, namely z-axis variation and the appearance of corners at the ellipse edges.

3.4 3D Film Structure with Randomly Located Voids

A 3D film specimen with randomly located voids and ϑ_f=0.50 experienced structural deformation and out-of-plane film motion upon uniaxial compression. At both levels of strain, all film domes

moved in the positive z-direction, with those clustered together experiencing greatest displacement. At 10% strain, the voids were no longer circular and appeared elliptical; with 20% strain, some of the voids became massively deformed, especially near the clustered area and at the base. Although void placement is not periodic, the film behaved predictably with respect to dome formation.

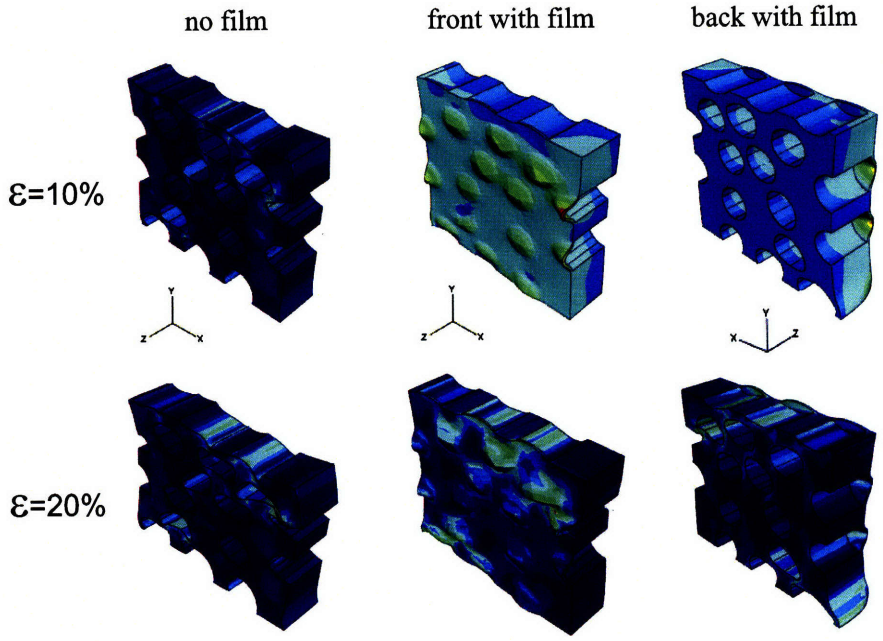

Figure 27: Images of non-film and film structures with randomly placed voids at 10 and 20% strain. The film behaves in a predictable manner and seems to have the greatest out-of-plane displacements in the void-clustered area and along the vertical edges.

4 Experimental

In an attempt to reproduce the simulations for validation and to generally view transformation in practice, a 3D specimen containing a bonded thin-film layer was experimentally loaded. The purchased 9.4 mm thick sheet of PSM-4 was transformed into a periodic array of ϑ_f 0.59 using a waterjet cutting machine. The thin film, also of PSM-4, was then bonded to the top surface of the structure using prescribed epoxy. Lastly, the final specimen (90 x 110 mm) was positioned in the experimental fixture and loaded to a maximum of about 13% strain.

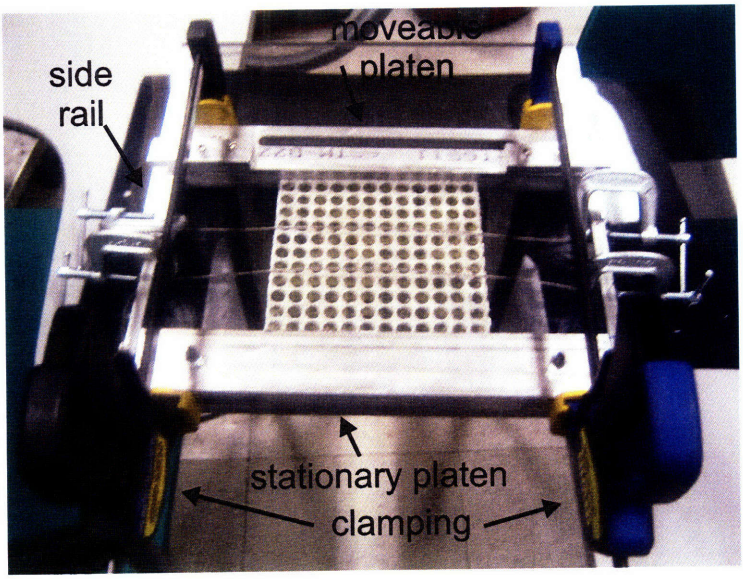

Figure 28: The experimental fixture used to load the 3D specimen with a thin-film layer. For loading, the clamping force was increased, translating the moveable platen closer to the stationary platen thus deforming the specimen. Cross cabling was used to suppress out-of-plane buckling.

4.1 Bonding of the Thin Film

Epoxy supplied by the Measurement Group was used to bond the thin-film to the periodic structure. Each bonding surfaces was first cleaned using both acetone and isopropyl alcohol. Next, a base layer of epoxy was applied to the structure's top surface and cured for two hours at approximately 150°C using an infrared lamp. Once the base coating had hardened, another epoxy layer was applied, and the film was positioned on top. The entire assembly was then allowed to cure at room temperature for thirty hours.

4.2 Experimental Loading Fixture

An experimental fixture was fabricated to allow for loading of the specimen. Fixture design proved difficult because compressive loading was required without constraining the film surface. The challenge was in suppressing the out-of-plane buckling mode while leaving the film free to deform. The final fixture design used for experimentation is shown in Fig. 28. As seen in the figure,

the approached used to suppress out-of-plane buckling was to string two steel cables[3] across the structure, in between arbitrary sets of void rows. This was deemed acceptably non-interfering because the cables would cross the structure in the channels created upon loading. The cables would provide a downward force as the structure deformed, forcing it into the plexiglas backing thus preventing buckling. Each cable was clamped into place by fixing each end to the side rails of the fixture. The rails were rigidly fixed to the stationary platen, but were free to move relative to the moveable platen. Loading was accomplished by increasing the clamping force which translated the moveable platen closer to the stationary one, thus deforming the structure. The specimen was loaded as far as about 13% strain and images of the results were captured through cross-polarizing sheets.

5 Experimental Results

Experimental loading of the film-structure specimen produced results which were predicted by the modeling simulations. Agreement is qualitative and approximate since many experimental challenges were encountered. Out of plane motion was handled well by the cross cabling, but it was still a source of frustration. It probably also contributed to film separation, which was seen in some areas. A more subtle but noticeable source of error was the slightly uneven and wavy edges of the structure. Despite such experimental imperfections, the outcomes were in agreement with simulation predictions and thus validate the modeling technique and results.

Figure 29 shows the loaded structure with no strain, 3.4%, 6.8%, 11.4%, and about 13% strain. The latter value is approximate since a precise measurement was not taken at this level. The coloring of the images comes from cross-polarizing sheets and is an indication of stress in the film; as strain progresses, the color patterns change. Regarding specific results, the figure shows that transformation occurs somewhere between 6.8% and 11.4% strain which spans the 9% transformation level predicted by Fig. 24. Note that transformation was not global as some of the voids remain circular,

[3]In Fig. 28, two cables were used for this larger structure of 119 x 130 mm; in the actual testing, a smaller specimen (90 x 110 mm) was loaded and only one cross cable was used.

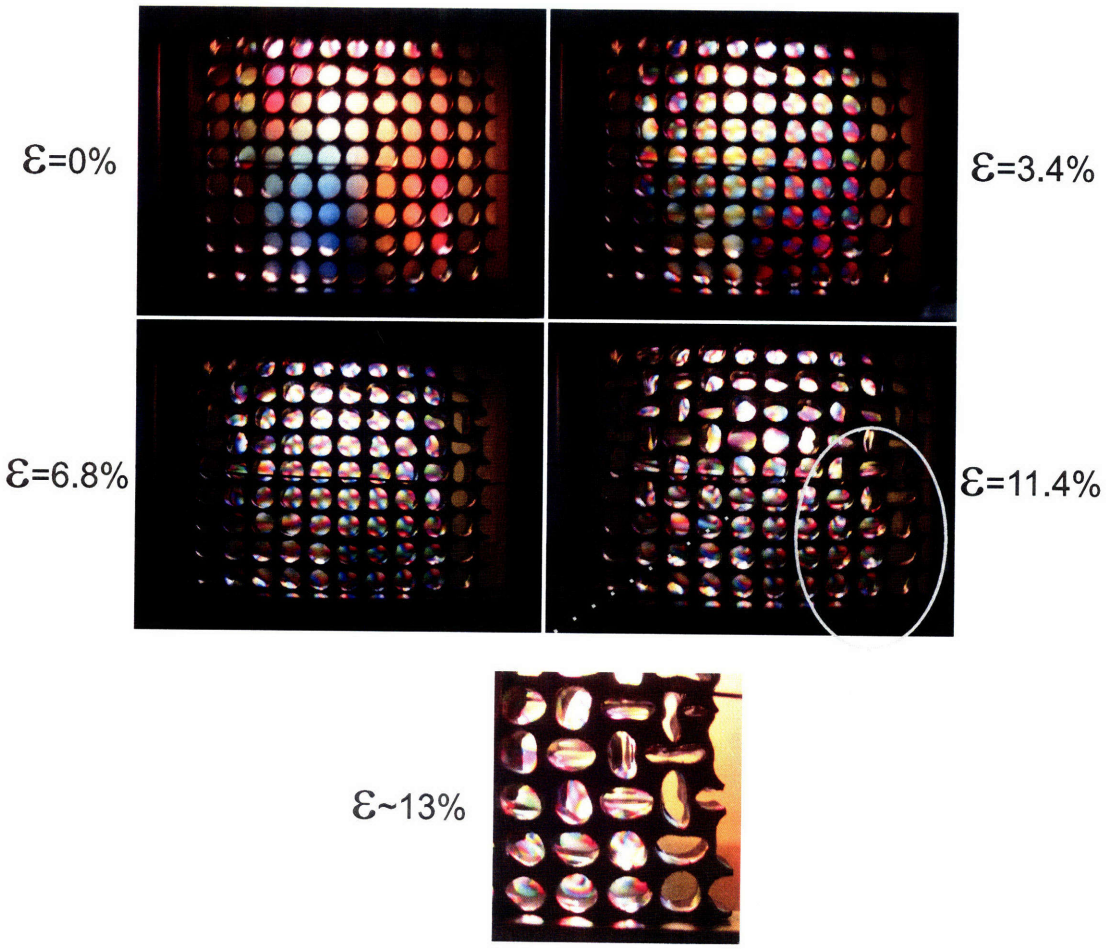

Figure 29: The loaded film structure at various levels of strain. The colors denote stress and are visualized by using cross-polarizing sheets. As expected, pattern transformation does not occur until after about 10% strain. These experimental results were in agreement with simulation predictions, and thus validate the model.

even at 11.4%. The regions which did not show transformation were actually at less strain since they had experienced out-of-plane global buckling.

In the image capturing 3.4% strain, film stress begins to develop in the lower righthand quadrant as is indicated by the purple color. This unsymmetric stress state is due to nonuniform loading of the structure. Despite nonuniformity, the raised domes can be felt at this level of strain. Further activity is seen with 6.8% strain imposed. The stress pattern is now more uniform, but intensity still favors the lower right quadrant. The domes continue out-of-plane motion and assume more spherical shapes; this is indicated by the colored X's crossing the voids. Those voids bonded to the film retain a circular shape–as is predicted by the stress-strain plot of Fig. 24–while the non-bound edge voids have become elliptical (recall that non-film 3D structures of ϑ_f 0.59 transform at around 5% strain (Fig. 19)).

By 11.4% strain, some of the bonded regions have begun transformation–mostly the left and right edges. Some ellipticity at this level seems accurate after referencing the stress-strain curve. Additionally, the crosses within the circular voids continue while polarized elliptical void patterns are more stress intense. The transformed structure is most visible in the sectional view of the lower right quadrant of the specimen. As expected, the non-film voids are massively deformed while some of the bonded voids are pinched horizontally and others are more circular. These results are accurate according to the visualizations of Fig. 25.

Even with some slight film separation, the experimental results were in agreement with modeling predictions. Qualitative behavior was accurate, and the stress-strain prediction was validated. In particular, transformation was shown to occur between 6.8% and 11.4%, spanning the 9% prediction. Additionally, raised domes were seen as early as 3.4% strain, supporting behavior shown in Fig. 24. If these or similar experiments are repeated in the future, a more robust method for preventing out-of-plane motion is required. Better film bonding is another area for improvement. To prevent film separation, an alternative bonding agent might be used, or the test specimen may be manufactured as one continuous piece.

6 Conclusions

The study of various periodic elastomeric structures has yielded behavioral understanding which has potential influence for implementation in practical devices. It was discovered that the three-dimensional specimens act like their 2D counterparts, and that addition of a thin film creates interesting deformed results for creating surface topology as well as influencing the underlying structure. Such behavior can be expected in practice since simulated predictions were verified experimentally.

The focal conclusion drawn from studying the 2D periodic structures is that a deformed alternating orthogonal ellipse pattern is found for volume fractions of 0.59 and 0.70 at the respective critical stress values. In moving from ϑ_f=0.59 to 0.70, critical stress decreases by a factor of about 7.7 (from 27 to 3.5 kPa) while the quantity $(\frac{t}{L})^2$ decreases by a factor of 6.4 (and is equal to 0.0899 and 0.0141 for ϑ_f 0.50 and 0.70, respectively). This quantity–where t is the ligament thickness (serving as an approximate measure of a column cross section dimension) and L is the void radius (serving as an approximate measure of a column length)–scales the critical buckling stress for column buckling [33]. In addition, when volume fraction is increased from 0.59 to 0.70, buckling occurs at lower stress and strain values. The decreased amount of material (quantified by the factor $(\frac{t}{L})^2$) with respect to ϑ_f 0.59 brings transformation at stress levels an order of magnitude lower. Apart from the similarly behaving 0.59 and 0.70 fractions, the specimens of ϑ_f 0.20 did not exhibit pattern transformation as a result of their material stability.

In moving to 3D structures, volume fraction 0.20 was no longer studied since it did not exhibit buckling. Results for ϑ_f 0.59 and 0.70, however, were in strong agreement with those of two dimensions. Major 2D observations were reproduced in these cases: The even-sized alternating ellipse pattern was seen and occurred at nearly constant levels of stress; volume fraction 0.70 also buckled faster and at lower stress values. In contrast, variations in buckling stress among even-sized mode 1 points was noted. Since the 2x2 ϑ_f 0.70 value could not be dismissed as analysis error and was farthest off, it was identified as a case needing further analysis.

Addition of the film yielded interesting model results but made experimentation slightly challenging. Simulations predicted a horizontal channel spanning the structure and located between rows of voids. They also showed considerable dome peak displacement where the rate of height increase was dependent upon strain regime. It was also noted that this rate decreased as transformation progressed. The presence of the film also postponed transformation and made it a more gradual process. Finally, the z-direction variation through the structure as well as the appearance of corners at void edges were attributed to film influence. Some of these observations were verified experimentally by loading a filmed structure of ϑ_f 0.59. Specifically, z-axis dome deformation was captured. The experimental component was also successful in verifying the stress-strain plot despite out-of-plane buckling and slight film separation. When the periodic voids were located randomly, simulations predicted that the film would show out-of-plane domes over the voids and that dome displacement was greater in void-clustered regions and along vertical edges.

7 Discussion

After summarizing main points in the previous section, there remain some open topics worthy of discussion. First, consider the results of loading an arbitrary (but within the limits of the study) 3D structure without constraining the top surface; it is very likely that the outcome would be different than that seen in the constrained case. With a free surface, out-of-plane buckling would have probably resulted, as was seen experimentally. Alternate third dimension effects would be possible, but unlikely. Apart from out-of-plane motion, there is not much potential for unpredicted outcomes. Once out-of-plane buckling is suppressed, the boundary conditions are as they were before. Another area for discussion is in practical applications for the structures. The ability to tailor and tune the surface topology has tremendous potential for practical implementation. It might be used for controllable friction at an interface or for water transport, utilizing the film channels. Completely sealed channels might be achieved with larger strain, a higher void-volume fraction, or the lack of film bonding over horizontal ligaments. Surface wettability could also be selected, switching from hydrophilic to repellent. The surface may also provide for special phononic

properties, granting the ability to accurately reflect light or to disperse it. Finally, a film structure with randomly located voids may be tunable so that surface topology can match environmental textures. In this way, objects fitted with such a surface would be camouflaged. The potential applications for the thin-film structures are attractive and are made more valuable by the ability to controllably switch surface topology. A product of the elastomeric properties of the material, this characteristic would be important for device adaptation and responsiveness.

References

[1] Tantikom K., Aizawa T., Mukai T., *International Journal of Solids and Structures* 2005, 42, 2199-2210.

[2] Tantikom K., Aizawa T., Mukai T., *International Journal of Solids and Structures* 2005, 42, 2211-2224.

[3] Bertoldi K., Boyce M.C., Deschanel S., Prange S.M., Mullin T., Mechanics of Deformation-Triggered Pattern Transformations and Superelastic Behavior in Periodic Elastomeric Structures, *J. Mech. Phys. Solids* 2008, in press.

[4] Parker A.R., McPhedran R.C., McKenzie D.R., Boten L.C., Nicorovici N.A.P., *Nature* 2001, 409, 36-37.

[5] Vukusic P., Sambles J.R., *Nature* 2003, 424, 852-855.

[6] Prum R.O., Quinn T., Torres R.H., *J. Exp, Biol.* 2006, 209, 748-765.

[7] Demp D.J., Vukusic P., Rutowski R.L., *Ecology* 2006, 282-289.

[8] Bertoldi K., Boyce M.C., Mechanically-Triggered Transformations of Phononic Band Gaps in Periodic Elastomeric Structures, *Physical Review B* 2008, 77, 052105.

[9] Quake S.R., Scherer A, *Science* 2000, 290, 1536-1540.

[10] Thorsen T., Roberts R.W., Arnold F.H., Quake S.R., *Phys. Rev. Lett.* 2001, 86, 4163-4166.

[11] Gao L.C., McCarthy T.J., *Langmuir* 2006, 22, 2966-2967.

[12] Bhushan B., Sayer R.A., *Microsyst. Technol.* 2007, 13, 71.

[13] Jagota A., Bennison S.J., *Am. Zool.* 2001, 41, 14831483.

[14] Crosby A.J.,Hageman M.,Duncan A., *Langmuir* 2005, 21, 1173811743.

[15] Rai-Choudhury P., *Handbook of Microlithography, Micromachining, and Microfabrication, SPIE Opt. Engineer. Press*, Bellingham, WA, 1997.

[16] Xia Y.N., Whitesides G.M., *Annu. Rev. Mater. Sci.* 1998, 28, 15318.

[17] Chaudhury M.K., Owen M.J., *Langmuir* 1993, 9, 29.

[18] Menezes P.L, Kishore, Kailas S.V., *Tribol. Lett.* 2006, 24, 265.

[19] Holmes D.P., Crosby A.J., *Adv. Mater.* 2007, 19, 3589-3593.

[20] Timoshenko S.P., Gere J.M., *Theory of Elastic Stability*, McGraw-Hill Book Company, New York, 2nd edn, 1961.

[21] Cerda E., Ravi-Chandar K., Mahadevan L., *Nature* 2002, 419, 579580.

[22] Vishay Measurements Group. Malvern, PA 19355-2143.

[23] Mullin T., Deschanel S., Bertoldi K., Boyce M.C., *Phys. Rev. Lett.* 2007, 99, 084301.

[24] Kinoshita S., Yoshioka S., *Chem. Phys. Chem.* 2005, 6, 1442-1459.

[25] Campbell M., Sharp D.N., Harrison M.T., Denning R.G., Tuberfield A.J., *Nature* 2000, 404, 53-56.

[26] Hennessy K., Reese C., Badolato A., Wang C.F., Imamoglu A., Petroff P.M., Hu E., *J. Vac. Sci. Technol.* 2003, B21, 2918-2921.

[27] Thylen L., Qiu M., Anand S., *Chem. Phys. Chem.* 2004, 5, 1268-1283.

[28] Ullal C.K., Maldovan M., Thomas E.L., Chen G., Han Y.J., Yang S., *Apply. Phys. Lett* 2004, 84, 5434-5436.

[29] Cheng J.Y., Mayes A.M., Ross C.A., *Nature Materials* 2004, 3, 823-828.

[30] Jang J.H., Ullal C.K., Tsukruk V.V., Thomas E.L., *Nano Letters* 2006, 6, 740-743.

[31] Choi T., Jang J.H., Ullal C.K., LeMieux M.C., Tsukruk V.V., Thomas E.L., *Advanced Functional Materials* 2006, 16, 1324-1330.

[32] Danielsson M., Parks D.M., Boyce M.C., Three Dimentional Micromechanical Modeling of Voided Polymeric Materials. *J. Mech. Phys. Solids* 2002, 50, 351-379.

[33] Crandall S., Dahl N., Lardner T., *An Introduction to The Mechanics of Solids.* McGraw Hill: New York, 1999.